2019

Estimating percentages of fusarium-damaged kernels in hard wheat by near-infrared hyperspectral imaging

Stephen R. Delwiche
USDA-ARS, stephen.delwiche@ars.usda.gov

I. Torres Rodriguez
Universidad de Cordoba - Spain

S. R. Rausch
USDA, Agricultural Research Service

R. A. Graybosch
USDA, Agricultural Research Service

Journal of Cereal Science 87 (2019) 18–24

Contents lists available at ScienceDirect

Journal of Cereal Science

journal homepage: www.elsevier.com/locate/jcs

Estimating percentages of fusarium-damaged kernels in hard wheat by near-infrared hyperspectral imaging☆

S.R. Delwiche[a,*], I. Torres Rodriguez[b], S.R. Rausch[a], R.A. Graybosch[c]

[a] USDA, Agricultural Research Service, Beltsville Agricultural Research Center, Food Quality Laboratory, 10300 Baltimore Avenue, Beltsville, MD, 20705-2350, USA
[b] Universidad de Córdoba, Campus de Rabanales, 14071, Córdoba, Spain
[c] USDA, Agricultural Research Service, Department of Agronomy, University of Nebraska, Lincoln, NE, 68583, USA

ARTICLE INFO

Keywords:
Wheat
Fusarium
Hyperspectral imaging

ABSTRACT

Fusarium head blight (FHB) is among the most common fungal diseases affecting wheat, resulting in decreased yield, low-density kernels, and production of the mycotoxin deoxynivalenol, a compound toxic to humans and livestock. Human visual analysis of representative wheat samples has been the traditional method for FHB assessment in both official inspection and plant breeding operations. While not requiring specialized equipment, visual analysis is dependent on a trained and consistent workforce, such that in the absence of these aspects, biases may arise among inspectors and evaluation dates. This research was intended to avoid such pitfalls by using longer wavelength radiation than the visible using hyperspectral imaging (HSI) on individual kernels. Linear discriminant analysis models to differentiate between sound and scab-damaged kernels were developed based on mean of reflectance values of the interior pixels of each kernel at four wavelengths (1100, 1197, 1308, and 1394 nm). Other input variables were examined, including kernel morphological properties and histogram features from the pixel responses of selected wavelengths of each kernel. The results indicate the strong potential of HSI in estimating fusarium damage. However, improvement in aligning this procedure to visual analysis is hampered by the inherent level of subjectivity in visual analysis.

1. Introduction

Fusarium head blight (FHB) is among the most common fungal diseases affecting wheat (*Triticum aestivum* L.). Primarily caused by *Fusarium graminearum*, this preharvest disease begins at the stage of flowering and lasts through grain fill (Parry et al., 1995; Dexter and Nowicki, 2003). Infected spikelets result in shriveled kernels that are chalky or pink in appearance. FHB reduces harvest yield due to decreased plant vigor and loss of low density kernels during threshing. From a food safety standpoint, FHB is a concern because of the often-associated synthesis of the secondary metabolite deoxynivalenol (aka DON, vomitoxin), a tricothecene mycotoxin, recently reviewed by Khaneghah et al. (2018). Human and livestock health risks of deoxynivalenol, such as toxemia, are well documented (Pestka and Smolinski, 2005), with the toxin also suspected of being a carcinogen (Ma et al., 2008). For more than a decade, most countries in the world have imposed maximum allowed levels of DON in raw and processed wheat for human consumption (van Egmond and Jonker, 2004; EC, 2006), typically ranging between 0.2 and 2 mg kg^{-1}, with baby foods having the most stringent limits.

Traditional methods for mycotoxin detection and measurement are based on immunology (e.g., ELISA, Rasmussen et al., 2003), chromatography (Trucksess et al., 1998), or chromatography with mass spectrometry (Sulyok et al., 2006). Although sensitive to concentration levels less than 1 mg kg^{-1}, these methods are not ideally suited to commercial grain inspection or plant breeding screening because of expense, complexity of operation, and time of analysis. As an alternative to measurement of the mycotoxin, the moldy appearance of the infected kernel is typically used in the screening of wheat genotypes. This process relies on the positive though imperfect correlation between the occurrence of the disease and the presence of the mycotoxin (Paul et al., 2005).

Human visual analysis of representative wheat samples has been the traditional method for fusarium damage assessment in both official inspection and plant breeding operations. While not requiring specialized equipment, visual analysis is dependent on a trained and

☆ Mention of trade names or commercial products in this publication is solely for the purpose of providing specific information and does not imply recommendation or endorsement by the U.S. Department of Agriculture. USDA is an equal opportunity provider and employer.

* Corresponding author.
E-mail address: stephen.delwiche@ars.usda.gov (S.R. Delwiche).

https://doi.org/10.1016/j.jcs.2019.02.008
Received 10 September 2018; Received in revised form 1 February 2019; Accepted 22 February 2019
Available online 28 February 2019
0733-5210/ Published by Elsevier Ltd.

consistent workforce, such that in the absence of these aspects, biases may arise among inspectors and evaluation dates. Visible and near-infrared spectroscopy has been examined as methods for detection of fusarium infection (Dowell et al., 1999; Pettersson and Aberg, 2003; Siuda et al., 2008; De Girolamo et al., 2009; Peiris et al., 2009, 2010). Color digital imaging for FDK was reported by Maloney et al. (2014) in which public access software (ImageJ) was used to assign the saturation level of each pixel within a digital image of a mass of kernels to either an infection or normal condition, whereupon the fraction of infected pixels to total pixels is used as an approximation to FDK.

The newest spectroscopy approach, hyperspectral imaging (described in the review of Gowen et al., 2007), utilizes digital images at comparatively narrow wavelength bands gathered over wavelength ranges covering the visible and short NIR region (400–1000 nm), the low wavelength section of the conventional NIR region (1000–1700 nm), or the full NIR region (1000–2500 nm). Desirable aspects of HSI imaging in commodity and food inspection include its automation potential, the scale-up potential for large throughput, and the ability to couple the technology to automatic sorting. Early HSI studies of grain involved differentiation of mold species (Penicillium, Aspergillus, and, Fusarium) in fungal-infected wheat kernels (Singh et al., 2007), wheat kernel discoloration (black point, field fungi, or pink stain) of Australian wheat kernels (Berman et al., 2007), classification of bulk samples of western Canadian wheat (Mahesh et al., 2008), and detection of insect damage in Canadian wheat (Singh et al., 2009). HSI reflectance studies on fusarium detection in wheat include those by Shahin and Symons (2011), who examined (400–1000 nm wavelength range) 800 kernels of Canada Western Red Spring wheat divided into three groups ranging in severity of fusarium damage, and by Barbedo et al. (2015), who studied (530–1780 nm range) a similar number (803) of kernels from four Brazilian wheat varieties spread across a similar arrangement of three groups. In early single kernel HSI transmission research on fusarium detection, Polder et al. (2005) drew two notable conclusions; first, the 900–1750 nm region was more accurate than the 430–900 nm region, and second, multivariate models using just a pair of wavelengths gave comparable results to more complex models involving latent variables derived from a full wavelength region. At the same time, Delwiche and Gaines (2005), working with single kernel reflectance from two spot-illuminated, fiber optic conveyance spectrometers arrived at the same conclusions as Polder's group. Elsewhere, Vermeulen et al. (2012) described the use of HSI to detect ergot bodies (sclerotia of the fungus *Claviceps purpurea*) among raw grain. Very recent work by Senthilkumar et al. (2017) documents the use of HSI to classify ochratoxin A (produced by *Penicillium* spp.) in stored wheat into five concentration levels, as well as a related study of same toxin in stored barley (Senthilkumar et al., 2016). A common feature of these HSI studies has been the limited number of kernels captured in a sample's image, often being fewer than 50, and often with kernels in precise alignment longitudinally and axially, which makes it difficult to estimate the level of damage of the lot from which the test sample was drawn. Herein, we release the restriction on kernel orientation and, at the same time, expand the number of kernels within a sample to more than 200. The objective of the current study has been to develop a near-infrared HSI procedure that identifies individual wheat kernels in bulk samples as sound or fusarium-damaged whereupon the percentage of fusarium-damaged kernels (FDK) is determined. An essential component of this objective is the selection of the statistical features (mean, median, standard deviation, skewness) or pixel histogram features of the wavelengths that are most successful in separating sound and damaged kernels.

2. Materials and methods

2.1. Wheat samples

Wheat was sourced from field plots at the University of Nebraska Havelock Farm, Lincoln, Nebraska (40.86° N, 96.61° W). Entries were planted in a randomized complete block design with three field replications in September 2014. Plot size was 3.7 m^2. Plots were fertilized with recommended rates for the site, using pre-plant applications. No fungicide was applied. Plots were harvested in-bulk by a mechanical research combine in July 2015. Entries included the cultivars Overland, Mace, Freeman, Panhandle, Settler CL and Mattern, plus 35 experimental breeding lines developed by USDA-ARS. Experimental lines included hard red, hard white, and waxy winter wheats. Altogether, 87 plot samples were studied, of which kernels from 5 samples were used to develop the spectral models, while the remaining 82 samples were used to test the models. In 2015, Fusarium infection in eastern Nebraska was severe (https://www.nebraskafarmer.com/wheat/whats-driving-nebraska-wheat-acres-down).

2.2. Instrumentation and data collection

The hyperspectral imaging system, assembled in the USDA Beltsville laboratory, consisted of an InGaAS focal-plane array camera, 320 × 256 pixels, 14-bit A/D (Xenics, Model Xeva-1.7-320, Leuven, Belgium), an imaging spectrograph (SWIR Hyperspec, Headwall Photonics, Fitchburg, MA, USA), two low-OH glass fiber optic bundles for conveying light from separate DC regulated 150 W quartz tungsten halogen light sources (Dolan Jenner, Model DC-950, Boxborough, MA, USA) to the imaging enclosure, and a stepper motor movable stage (Velmex, Model XN10-0180-M02-21, Bloomfield, NY, USA) that moved the imaged seeds across the line field of view of the camera. The termini of the fiber bundles were single fibers arranged in 250 mm long slits positioned parallel to the camera's line field of view and approximately 250 mm above the image surface. Emanating light from the two bundles was directed downward at opposing nominal angles of 30° from the vertical, with intersection at approximately 10 mm above the image surface to minimize shadowing. A 25-mm zoom lens (Optec, Model OB-SWIR25/2, Parabiago, Italy) was connected to the front end of the spectrograph. With a working distance of 240 mm (front of lens to object surface), the actual field of view width was 90 mm, equivalent to the width of the rectangular specimen tray. To maintain square pixels, the step distance of the stage was set at 0.29 mm, thus requiring 470 lines to span the 136-mm length of the specimen tray. The effective wavelength range was 938–1654 nm, and with 150 spectral bands (hereafter called wavelengths) collected, the average spacing between wavelengths was 4.8 nm. Spectral data was stored in two-byte integer format in an array of dimensions 320 × 470 × 150 and later converted to 8-byte floating point format for mathematical operations. Additional detail on the spectral and spatial calibration of the system is found in Kim et al. (2012).

A dark current intensity image was collected on an hourly basis (approximately after every 10 samples) by covering the camera lens. Likewise, intensity from a 99% reflectance standard, consisting of sintered PTFE (Spectralon™, SRT-99-120, Labsphere, North Sutton, NH, USA), was collected immediately after the dark current image. These two images were applied to the subsequent sample intensity images until the next pair of dark current and white reflectance images. For the five samples used to develop the classification models, kernels were manually sorted by one trained technician into sound and fusarium-damaged groups before scanning. Kernels that were visually shriveled or chalky in appearance were designated as fusarium-damaged kernels (FDK) and placed in the middle region of the specimen tray, with care taken to avoid touching occurrences. The non-touching sound kernels were placed on both sides of the middle region, such that as the stage was advanced during imaging, a zone containing half of the sound kernels was scanned first, followed by the middle zone containing all the sample's fusarium-damaged kernels and the trailing zone containing the remaining half of the sound kernels. This intentional arrangement was performed to ensure that the proper assignment of sound and fusarium-damaged kernels during model development. The orientation

about each kernel's axis (e.g., crease up, down, or side) was random.

For the 82 samples reserved for model validation, manual visual sorting was not performed before scanning. Instead, the kernels were spread out in random orientation on the specimen tray, again with care taken to minimize instances of touching kernels. Typically, between 200 and 250 kernels comprised each 4-g sample in the test set. Upon scanning, each of the 82 test set samples was returned to an envelope for later visual sorting. Sorting was performed by the same technician who sorted the calibration kernels. Count percentages of fusarium-damaged kernels [%FDK = 100 × (number of FDK)/(number of FDK + number of sound)] were determined for comparison to model predictions.

For both calibration and test samples, photographs were taken of the trays immediately before HSI scanning event using a digital single lens reflex. JPEG images of the samples were later used for two purposes: first, to verify object identification in the calibration set trays during image processing and second, to allow for the spot checking of classification assignments by having the technician view a sample's photo and make *a posteriori* assignment of each kernel into sound or fusarium-damaged condition.

2.3. Hyperspectral image processing

Images of a representative sample are shown in Fig. 1, starting with a photograph of the sample taken immediately before scanning (top pane). Data reduction and spectral analysis tasks were performed in MATLAB (v. 2016a) equipped with the image processing toolbox. The intensity readings of each test sample's data array were transformed to reflectance by dividing the dark current-subtracted intensity by the dark current-subtracted white standard intensity at each of the corresponding wavelengths (i.e., image slices), with the result shown by example in the middle pane of Fig. 1. For removing the emery cloth background, all pixels having reflectance at the tenth wavelength (981 nm) less than 0.2 were set to 0, and the remaining pixels were set to 1. This mask was then applied to all slices in the data array. Using the image at 981 nm, object boundaries were eroded using a disk-shaped structuring element of radius 1 to reduce the effect of oblique surfaces. The eroded image is seen by example in the bottom pane of Fig. 1. Following erosion, relevant objects were identified as contiguous regions of 30 or more pixels. Smaller regions, often broken pieces of kernel, were discarded. Objects of greater than 300 pixels, indicative of two or more touching kernels, were likewise discarded.

2.4. Spectral analysis

Each identified object from image processing, hereafter termed a kernel, was initially reduced to a mean reflectance spectrum by averaging the pixel reflectances within the kernel. Partial least squares discriminant analysis (PLSDA) calibrations were developed (proc PLS in SAS, *SAS Institute Inc., Cary, NC, USA*) on the mean spectra using assigned reference values of 0 and 1 for sound and fusarium-damaged kernels, respectively, with 0.5 as the boundary between these two conditions. Spectral preprocessing (smooths, normalizations) was not performed (other than mean-centering) except in the case of one trial which used a standard normal variate (SNV) transformation (Barnes et al., 1989). The purpose of the PLSDA modeling was to establish the limits of model accuracy for the evaluation of subsequent linear discriminant analysis (LDA) models employing a much smaller number of wavelengths as a precursor to a multispectral design.

For each of the five calibration samples, whose mass was approximately 4 g, the number of sound kernels always exceeded the number of FDK. Therefore, despite the entire tray being scanned, not all sound kernels were used in calibration development. Instead, the number of sound kernels used in each calibration sample was set to the number of fusarium-damaged kernels, with half this number located in leading region and the other half in the trailing region. Altogether, 278

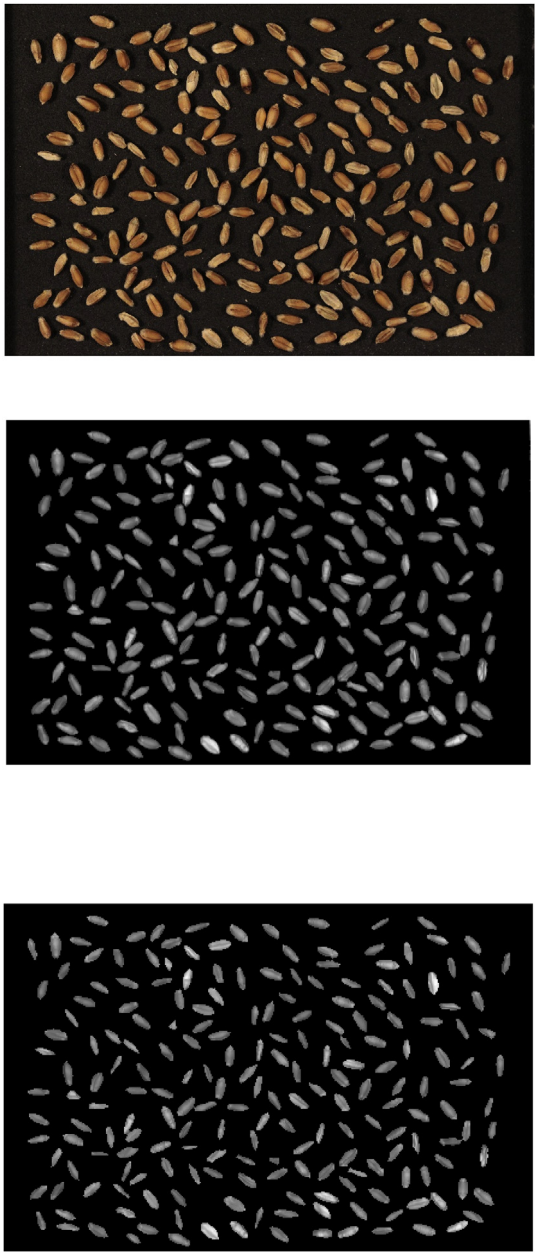

Fig. 1. Photo of a representative sample (top), along with the tenth image slice (981 nm) from its hyperspectral data array, before (middle), and after masking and erosion operations (bottom).

fusarium-damaged kernels and an equal number of sound kernels comprised the calibration set. The number of pixels per kernel after erosion, synonymous with kernel area, varied from 30 to 223 for sound kernels (median = 81), and 35 to 141 for fusarium-damaged kernels (median = 81), with the large variation within a condition attributed to the genetic diversity of the field samples. Pixel spectra within a kernel were reduced to produce a mean spectrum and other statistical summary properties (median, standard deviation, skewness, kurtosis). Reflectance values of a kernel's pixels were also binned to produce histogram features at each wavelength.

Development of the LDA models consisted of an exhaustive search (proc DISCRIM in SAS) of the pixel mean reflectances across the entire spectral range to identify the pair of wavelengths, when combined with the wavelength at 1000 nm (for baseline referencing), that produced the greatest number of correctly classified calibration set kernels. This was repeated when a fourth wavelength was included. In addition to

the analyses involving kernel mean spectra, other LDA spectral modeling trials included a) the raw pixel reflectances sorted into bins of 0.1 successive increments for each of the 3–4 identified wavelengths, in which searches (proc STEPDISC in SAS) of the best bins or summation of bins were conducted in a stepwise manner; and b) median, standard deviation, skewness, and kurtosis of the raw pixel values of the 3–4 wavelengths.

In addition to spectral PLSDA and LDA models, elementary morphological properties of the masks were examined in LDA modeling. The properties were area = kernel pixel count, solidity = area divided by area of the smallest convex polygon encompassing the kernel, eccentricity = distance between foci of the ellipse of matching normalized second central moment divided by major axis length of the ellipse, and ellipse minor axis length divided by major axis length. An LDA classification model based on all five morphological properties was developed using the same kernels for calibration as used in spectral modeling. For either spectral or morphological LDA models, assessment of a calibration was first evaluated by one-kernel-out cross-validation accuracy, in which kernels identified as sound or fusarium-damaged were tallied and the counts were referenced to their visual identification. The better calibrations were then tested on the validation samples.

For the validation samples (n = 82, average kernel count = 254, mean %FDK = 18.7 units, standard deviation %FDK = 8.6 units), tallies of model-determined sound and fusarium-damaged kernels were made for each sample. Validation accuracy was estimated by comparison to the percentages by visual analysis; however, true validation at the individual kernel level was not possible because visual assessment was not performed *in situ* (i.e., while kernels were still on the tray). Therefore, kernels identified as fusarium-damaged by the model may not have been the same kernels identified in visual analysis, and likewise for the sound kernels. To address the level of uncertainty caused by improper assignment, the validation set samples were visually analyzed a second time by the same technician 20 months after the first visual analysis. Although the second analysis still does not corroborate classification assignment at the individual kernel level, it serves to estimate the uncertainty error of the reference procedure, with the understanding that such error propagates through the model.

3. Results

Fusarium-damaged kernels tended to have greater reflectance across the entire wavelength region than sound kernels, as demonstrated by their grand mean spectra in Fig. 2. Although a lack of overlap of the ± 1 standard deviation envelopes across a large portion of the wavelength region suggests that the two categories are spectrally separable using as few as one wavelength. However, assuming equal normal distributions between the categories at a given wavelength, the closeness of the interior envelope lines suggests that more than 16% (i.e., tail beyond 1σ) of the kernels would be misclassified by a one-wavelength model. Also apparent from the reflectance spectra is the lack of sharp absorption regions. Instead, there are local maxima near 1100 nm and 1300 nm, and local minima near 1000 nm, 1200 nm and 1430 nm, as seen by the grand mean difference spectrum (sound minus fusarium-damaged). Prior research on near-IR spectral characteristics of fusarium fungi by conventional spectroscopy indicated possible absorption bands from ergosterol ($C_{28}H_{44}O$) and chitin [$(C_8H_{13}O_5N)_n$], fungal cell mass produced from metabolism of the endosperm (Dowell et al., 1999). Our earlier research that examined HSI spectra of purified forms of ergosterol and chitin indicated absorption bands near 1200 nm and 1480 nm, respectively.

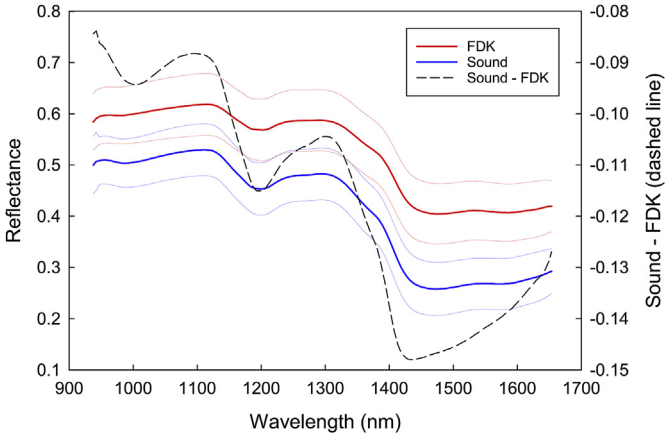

Fig. 2. Means of kernel mean spectra of FDK and Sound kernels (n = 278 for each group), along with ± 1 standard deviation envelope. Also included is the difference spectrum formed as the sound mean minus the FDK mean (scaled on right axis).

With one wavelength term fixed at 1000 nm, the exhaustive search of two additional wavelengths for yielding the best cross-validation accuracy on the 576-kernel calibration set is shown in the contour plot of Fig. 3. The region that produced the highest accuracy consisted of a wavelength near 1400 nm and a second wavelength spanning between 1200 and 1300 nm. Within this region, the two best wavelengths were 1197 nm and 1394 nm. Absorption at the smaller of these wavelengths is attributed to ergosterol, while the larger wavelength (1394 nm) is close to 1405 nm, which Williams et al. (2012) found important in hyperspectral image analysis of corn inoculated with *Fusarium verticillioides*. It is also close to 1411 nm, the wavelength that Barbedo et al. (2015) found to provide the best separation between sound and fusarium-damaged wheat kernels.

The summaries of the cross-validation classification results are shown in Table 1. Accuracies, defined as the percentages of correctly identified sound or fusarium-damaged kernels during a leave-one-out cross-validation procedure, are shown for PLSDA (2, 4, and 7 factors), sets of chosen wavelengths (2, 3, and 4 wavelengths), and one set of morphological properties. With either the PLSDA or multiple regression approach, the accuracies were always greater than 92%. Two factors were optimal for the PLSDA approach, giving an overall accuracy of 97.3%. Four wavelengths (1100 nm, 1197 nm, 1308 nm, and 1394 nm) produced nearly the same level of accuracy (overall 96.8%). At such a small difference in accuracy of the two approaches, the multiple regression (discrete wavelength) approach is considered more desirable because it may be applied to a multispectral design (instead of hyperspectral), with the advantages of reduced processing time and less expensive hardware. Also, included in this table are the cross-validation accuracies of the four-wavelength median reflectance model. Compared to the mean reflectance model using the same four wavelengths, the median model had a slightly lower cross-validation accuracy (94.6% vs. 96.8%). The corresponding accuracies of the two and three wavelength median models were on par with their mean counterparts (data not shown). Because the model based on morphological properties, with a mean accuracy of 50.9%, was much poorer than the spectral properties models, no further evaluation of morphological properties was pursued. Additionally, models that used either a) SNV-transformation prior to best wavelength searches of mean reflectances, b) histogram bins of reflectances or their accumulated sum, c) statistical properties characterizing the shape of a kernel's pixel reflectance distribution (standard deviation, skewness, and kurtosis) at the 3–4 previously identified best mean wavelengths, were all inferior to the spectral mean (and in one case, spectral median) models summarized in Table 1. Therefore, these inferior models were not explored further.

Table 1 also contains the validation results of the corresponding PLSDA and discrete wavelength models. The standard errors of prediction (SEP, defined as the standard deviation of modeled percentage of FDK minus visual percentage of FDK) ranged from 4.9 to 6.6 percentage units, while the bias terms were more widely varying (−8.7 to 9.0 percentage units). The four-wavelength (1000, 1197, 1308 and 1394 nm) means model validation set predictions are plotted in Fig. 4,

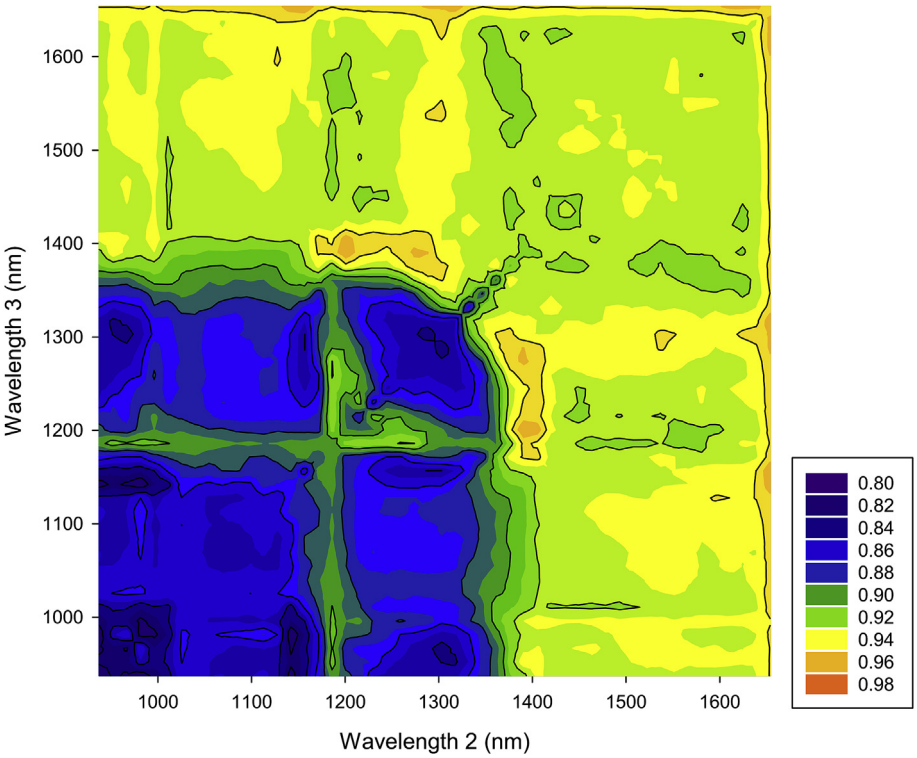

Fig. 3. Contour plot of cross-validation accuracies of linear discriminant analysis models involving mean kernel reflectances at three wavelengths, with one wavelength fixed at 1000 nm, using the calibration set consisting of 278 sound kernels and 278 fusarium-damaged kernels.

demonstrating Pearson product-moment and Spearman rank-order correlations of 0.772 and 0.811, respectively. Either by visual analysis or by HSI model, the percentage of FDK ranged from slightly less than 10% to approximately 40%. As with all spectral regression models, model accuracy is ultimately dependent on the accuracy of the reference procedure, which for this study is human visual analysis. One way to estimate the reference error was through the recounting of sound and fusarium-damaged kernels of the validation samples. We found that the standard deviation of the differences of the %FDK between the initial count and the recount was 5.7 percentage units. Because this value is equivalent to the SEP values of Table 1, further improvement in the HSI models is not possible because of the inherent variation in the reference visual analysis.

Another approach for checking model performance at the kernel level is by comparing HSI classification assignments with visual assignments of the digital photographs. This is shown for only one validation set sample (Fig. 5), acknowledging the earlier mentioned limitations of the use of the photographs for FDK assessment. In Fig. 5, assignments by the 4-wavelength kernel mean LDA model are shown by graph of the centroid locations of each kernel using a symbol to indicate the model's assignment of sound (−) or FDK (+). With the digital photograph shown in the upper half of the figure, we observe that while

Table 1
Results of sound vs. fusarium-damaged kernel classification by partial least squares discriminant analysis (PLSDA, with number of latent variables, LVs, noted) or linear discriminant analysis (LDA, on wavelengths or morphological properties noted) on cross-validation and external validation sets.

Model	Cross-Validation on 278 Sound Kernels and 278 Fusarium-Damaged Kernels		Validation on 82 External Samples (each sample containing 198–250 kernels)	
	Number of Correctly Classified Sound Kernels (percent)	Number of Correctly Classified Fusarium-Damaged Kernels (percent)	SEP[a] (percentage units)	Bias[b] (percentage units)
PLSDA, 2 LVs	268 (96.4)	273 (98.2)	6.47	8.11
PLSDA, 4 LVs	260 (93.5)	267 (96.0)	5.91	−0.24
PLSDA, 7 LVs	261 (93.9)	257 (92.4)	6.46	−8.66
LDA, 1197 nm, 1394 nm	262 (94.2)	262 (94.2)	6.63	8.97
LDA, 1000 nm, 1197 nm, 1394 nm	267 (96.0)	267 (96.0)	6.31	2.12
LDA, 1000 nm, 1197 nm, 1308 nm, 1394 nm	270 (97.1)	268 (96.4)	5.76	−0.25
LDA, 1000 nm, 1197 nm, 1308 nm, 1394 nm[c]	263 (94.6)	263 (94.6)	4.87	1.93
LDA, area, solidity, eccentricity, mima[d]	133 (47.8)	150 (54.0)	—	—

[a] SEP = standard error of prediction (= standard deviation of residuals).
[b] Bias = mean of modeled values minus mean of visual analysis values.
[c] Based on median reflectance value of each of the four wavelengths, as opposed to the preceding line in table, in which mean reflectance values were used.
[d] area = kernel pixel count; solidity = area divided by area of the smallest convex polygon encompassing the kernel; eccentricity = distance between foci of the ellipse of matching normalized second central moment divided by major axis length of the ellipse; mima = ellipse minor axis length divided by major axis length.

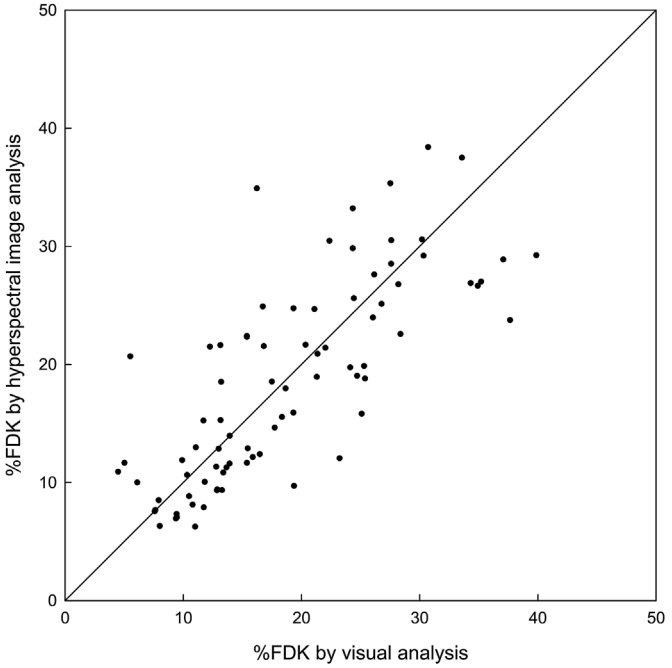

Fig. 4. Scatter plot of the predictions of fusarium-damaged kernel percentages by linear discriminant analysis using four reflectances as predictor variables (1000 nm, 1197 nm, 1308 nm, 1394 nm) versus the percentages determined by human visual analysis.

a large majority of the sound kernels agreed between the two methods, some of the kernels identified by HSI as being fusarium-damaged were not considered as such when the color photograph was evaluated, but because some sound kernels by HSI were identified as fusarium-damaged in the photograph, the overall FDK value for that sample was in agreement between the two procedures. Compared to the earlier description of the recounting of the actual kernels, the potential advantage of this approach is the one-to-one correspondence at the kernel level. However, the disadvantage of the approach is the inability to observe the entire kernel surface in the photograph.

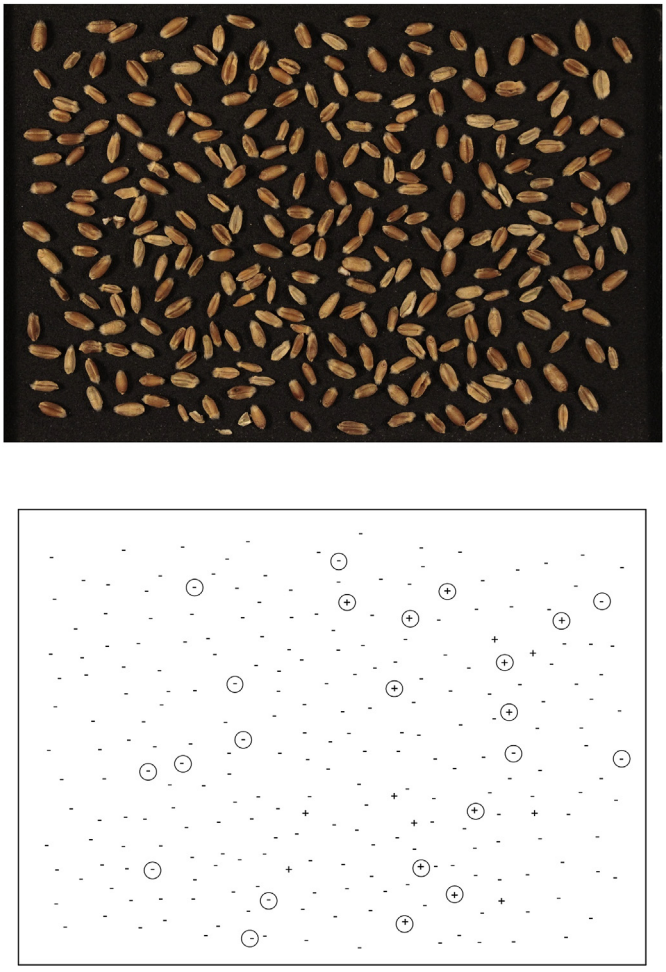

Fig. 5. Corroboration of four wavelength (1000 nm, 1197 nm, 1308 nm, 1394 nm) mean kernel classification model applied to one representative validation sample with visual analysis of the sample's color digital photograph. Minuses (−) and pluses (+) are HSI-classified sound and fusarium-damaged kernels, respectively. Circles indicate disagreement between HSI and visual assignments. (For interpretation of the references to color in this figure legend, the reader is referred to the Web version of this article.)

4. Discussion

The results of the classification modeling indicate the strong potential of HSI in determining FDK. At the same time, however, improvement in aligning this procedure to visual analysis is hampered by the inherent level of subjectivity in visual analysis. Maloney et al. (2014) proposed an alternative using color digital imaging by treating a sample as a continuous mass instead of discrete kernels, whereupon the level of fusarium damage is equated to the proportion of pixels in an image whose saturation values are within a user-determined range. Such an approach requires periodic readjustment of the range with the onset of a new season, different varieties, or other changes in environmental conditions that affect kernel color. By using wavelengths longer than that of the visible region, the current study may be less prone to the environmental conditions that affect the appearance of the fusarium-damaged kernel, hence the need for fine tuning to genotype and yearly growing conditions may not be needed; however, this becomes a difficult concept to prove given the underlying referencing of the procedure is visual analysis. On a test set of 200 sound and 200 fusarium-damaged Canada western red spring wheat kernels, Shahin and Symons (2011) achieved an overall accuracy of 92% using a principal component scores from HSI data collected over a 400–1000 nm range. The level of accuracy was maintained at 92% when six discrete wavelengths (484 nm, 567 nm, 684 nm, 817 nm, 900 nm, and 950 nm, with selection based on local minima and maxima of the first five PC loadings) were used instead of the PC scores. The closest comparison between Shahin and Symons' findings and those of the current study is made with their calibration set results (also performed by LDA of principal component scores or discrete wavelengths on a set of 400 kernels evenly divided between sound and fusarium-damaged) and the current study's cross-validation PLSDA and discrete wavelength LDA results (on 556 kernels, also evenly divided) in Table 1. The corresponding accuracies of the Shahin and Symons' (400–1000 nm region) study and the current (940–1659 nm region) study were 92–93% and 93–97%, respectively. While the current study's accuracy is slightly higher, perhaps because of reliance on the near-IR region, direct comparison is tenuous because of the different sample sets and inevitable differences in the trained technicians who performed the reference analyses.

In summary, the HSI results herein suggest that a multispectral imaging system consisting of three or four wavelength filters is capable of estimating FDK to the extent of the accuracy of the underlying visual inspection procedure. Additionally, to the extent of the relationship between fusarium damage and deoxynivalenol occurrence, a multispectral system coupled with a sorter could be used to identify and remove the damaged kernels and, in so doing, lower the mycotoxin concentration. The level of such lowering is reserved for future research. Further, based on the success of Barbedo et al. (2015) at

separating lightly touching kernels by image processing (thus reducing the requirement of separation by physical operation), fusarium-damage assessment of breeders' stock by a line-scan HSI, moving conveyer belt system, is a reasonable expectation for future development. Scale-up for commercial operations in elevators and mills, however, is a far more daunting challenge.

5. Conclusions

Linear discriminant analysis (LDA) of mean reflectance values of the interior pixels of kernels scanned by NIR hyperspectral imaging identified four wavelengths (1100, 1197, 1308, and 1394 nm) as sufficient for differentiating sound and fusarium-damaged kernels. While cross-validation accuracy was high (> 95%) on the individual kernel level for kernels of high visual contrast between sound and fusarium-damaged condition, true model accuracy, when evaluated on external samples, is lessened because of the ambiguous appearance of some kernels. With respect to spectral imaging of wheat kernels for fusarium damage, we conclude that a) classification models need only be based on 4 wavelength filters in a multispectral design, b) kernels in a spectral sample may be randomly arranged, and c) an imaging procedure may operate on several hundred kernels at once (or on a moving line), thus reducing the processing time to the order of milliseconds per kernel.

Conflicts of interest

The authors have no conflict of interest regarding the content of this paper.

Appendix A. Supplementary data

Supplementary data to this article can be found online at https://doi.org/10.1016/j.jcs.2019.02.008.

References

Barbedo, J.G., Tibola, C.S., Fernandes, J.M., 2015. Detecting Fusarium head blight in wheat kernels using hyperspectral imaging. Biosyst. Eng. 131, 65–76.

Barnes, R.J., Dhanoa, M.S., Lister, S.J., 1989. Standard normal variate transformation and de-trending of near-infrared diffuse reflectance spectra. Appl. Spectrosc. 43, 772–777.

Berman, M., Connor, P.M., Whitbourn, L.B., Coward, D.A., Osborne, B.G., Southan, M.D., 2007. Classification of sound and stained wheat grains using visible and near infrared hyperspectral image analysis. J. Near Infrared Spectrosc. 15, 351–358.

De Girolamo, A., Lippolis, V., Nordkvist, E., Visconti, A., 2009. Rapid and non-invasive analysis of deoxynivalenol in durum and common wheat by Fourier-Transform Near Infrared (FT-NIR) spectroscopy. Food Addit. Contam. 26, 907–917.

Delwiche, S.R., Gaines, C.S., 2005. Wavelength selection for monochromatic and bichromatic sorting of fusarium-damaged wheat. Appl. Eng. Agric. 21, 681–688.

Dexter, J.E., Nowicki, T.W., 2003. Safety assurance and quality assurance issues associated with Fusarium head blight in wheat. In: Leonard, K.J., Bushnell, W.R. (Eds.), Fusarium Head Blight of Wheat and Barley. APS Press, St. Paul, MN, USA, pp. 420–460 530 pp.

Dowell, F.E., Ram, M.S., Seitz, L.M., 1999. Predicting scab, vomitoxin, and ergosterol in single wheat kernels using near-infrared spectroscopy. Cereal Chem. 76, 573–576.

EC, 2006. Commission Regulation (EC) No 1881/2006 of 19 December 2006 setting maximum levels for certain contaminants in foodstuffs. In: Official Journal of the European Union.

Gowen, A.A., O'Donnell, C., Cullen, P.J., Downey, G., Frias, J.M., 2007. Hyperspectral imaging–an emerging process analytical tool for food quality and safety control. Trends Food Sci. Technol. 18, 590–598.

Khaneghah, A.M., Martins, L.M., von Hertwig, A.M., Bertoldo, R., Sant'Ana, A.S., 2018. Deoxynivalenol and its masked forms: characteristics, incidence, control and fate during wheat and wheat based products processing-A review. Trends Food Sci. Technol. 71, 13–24.

Kim, M.S., Delwiche, S.R., Chao, K., Garrido-Varo, A., Perez-Marin, D., Lefcourt, A.M., Chan, D., 2012. Visible to SWIR hyperspectral imaging for produce safety and quality evaluation. In: Sensing and Instrumentation for Food Quality and Safety, vol. 5. pp. 155–164.

Ma, Y.Y., Guo, H.W., 2008. Mini-review of studies on the carcinogenicity of deoxynivalenol. Environ. Toxicol. Pharmacol. 25, 1–9.

Mahesh, S., Manickavasagan, A., Jayas, D.S., Paliwal, J., White, N.D.G., 2008. Feasibility of near-infrared hyperspectral imaging to differentiate Canadian wheat classes. Biosyst. Eng. 101, 50–57.

Maloney, P.V., Petersen, S., Navarro, R.A., Marshall, D., McKendry, A.L., Costa, J.M., Murphy, J.P., 2014. Digital image analysis method for estimation of Fusarium-damaged kernels in wheat. Crop Sci. 54, 2077–2083.

Parry, D.W., Jenkinson, P., McLeod, L., 1995. Fusarium ear blight (scab) in small grain cereals—a review. Plant Pathol. 44, 207–238.

Paul, P.A., Lipps, P.E., Madden, L.V., 2005. Relationship between visual estimates of Fusarium head blight intensity and deoxynivalenol accumulation in harvested wheat grain: a meta-analysis. Phytopathology 95, 1225–1236.

Peiris, K.H.S., Pumphrey, M.O., Dowell, F.E., 2009. NIR absorbance characteristics of deoxynivalenol and of sound and Fusarium-damaged wheat kernels. J. Near Infrared Spectrosc. 17, 213–221.

Peiris, K.H.S., Pumphrey, M.O., Dong, Y., Maghirang, E.B., Berzonsky, W., Dowell, F.E., 2010. Near-infrared spectroscopic method for identification of Fusarium head blight damage and prediction of deoxynivalenol in single wheat kernels. Cereal Chem. 87, 511–517.

Pestka, J.J., Smolinski, A.T., 2005. Deoxynivalenol: toxicology and potential effects on humans. J. Toxicol. Environ. Health, Part B 8, 39–69.

Pettersson, H., Åberg, L., 2003. Near infrared spectroscopy for determination of mycotoxins in cereals. Food Control 14, 229–232.

Polder, G., Van Der Heijden, G.W.A.M., Waalwijk, C., Young, I.T., 2005. Detection of Fusarium in single wheat kernels using spectral imaging. Seed Sci. Technol. 33, 655–668.

Rasmussen, P.H., Ghorbani, F., Berg, T., 2003. Deoxynivalenol and other Fusarium toxins in wheat and rye flours on the Danish market. Food Addit. Contam. 20, 396–404.

Senthilkumar, T., Jayas, D.S., White, N.D., Fields, P.G., Gräfenhan, T., 2016. Detection of fungal infection and Ochratoxin A contamination in stored barley using near-infrared hyperspectral imaging. Biosyst. Eng. 147, 162–173.

Senthilkumar, T., Jayas, D.S., White, N.D.G., Fields, P.G., Gräfenhan, T., 2017. Detection of ochratoxin A contamination in stored wheat using near-infrared hyperspectral imaging. Infrared Phys. Technol. 81, 228–235.

Shahin, M.A., Symons, S.J., 2011. Detection of Fusarium damaged kernels in Canada Western Red Spring wheat using visible/near-infrared hyperspectral imaging and principal component analysis. Comput. Electron. Agric. 75, 107–112.

Singh, C.B., Jayas, D.S., Paliwal, J., White, N.D.G., 2007. Fungal detection in wheat using near-infrared hyperspectral imaging. In: Transactions of the ASABE, vol. 50. pp. 2171–2176.

Singh, C.B., Jayas, D.S., Paliwal, J., White, N.D.G., 2009. Detection of insect-damaged wheat kernels using near-infrared hyperspectral imaging. J. Stored Prod. Res. 45, 151–158.

Siuda, R., Balcerowska, G., Kupcewicz, B., Lenc, L., 2008. A modified approach to evaluation of DON content in scab-damaged ground wheat by use of diffuse reflectance spectroscopy. Food Anal. Meth. 1, 283.

Sulyok, M., Berthiller, F., Krska, R., Schuhmacher, R., 2006. Development and validation of a liquid chromatography/tandem mass spectrometric method for the determination of 39 mycotoxins in wheat and maize. Rapid Commun. Mass Spectrom. 20, 2649–2659.

Trucksess, M.W., Page, S.W., Wood, G.E., Cho, T.H., 1998. Determination of deoxynivalenol in white flour, whole wheat flour, and bran by solid-phase extraction/liquid chromatography: interlaboratory study. J. AOAC Int. 81, 880–886.

van Egmond, H.P., Jonker, M.A., 2004. Worldwide Regulations for Mycotoxins in Food and Feed in 2003. Food and Agriculture Organization of the United Nations.

Vermeulen, P., Pierna, J.F., Egmond, H.V., Dardenne, P., Baeten, V., 2012. Online detection and quantification of ergot bodies in cereals using near infrared hyperspectral imaging. Food Addit. Contam. A 29, 232–240.

Williams, P.J., Geladi, P., Britz, T.J., Manley, M., 2012. Investigation of fungal development in maize kernels using NIR hyperspectral imaging and multivariate analysis. J. Cereal. Sci. 55, 272–278.